J. Fluid Mech. (2014), *vol.* 754, R1, doi:10.1017/jfm.2014.397

JFM RAPIDS
journals.cambridge.org/rapids

On the cusps bordering liquid sheets

J. M. Gordillo[1], H. Lhuissier[2] and E. Villermaux[3,†]

[1]Área de Mecánica de Fluidos, Departamento de Ingeniería Aeroespacial y Mecánica de Fluidos, Universidad de Sevilla, Avenida de los Descubrimientos s/n 41092, Sevilla, Spain

[2]Université Paris Diderot, CNRS, Matière et Systèmes Complexes UMR 7057, 75205 Paris, France

[3]Aix Marseille Université, CNRS, Centrale Marseille, IRPHE UMR 7342, 13384 Marseille, France

(Received 11 March 2014; revised 22 May 2014; accepted 8 July 2014)

The edge of a stationary radially expanding liquid sheet and the receding rim bordering a plane sheet are naturally indented. It presents a collection of cusps at the extremity of which the liquid concentrates and is expelled. An experimental description of these cusps for a stationary flat inviscid Savart sheet is given. We identify the stable node–jet structure responsible for the deflection of the incoming flow at the rim and demonstrate how these cusps are the structures that accommodate for both mass and momentum conservation at the sheet edge. Their shape, their number around the sheet, and the residual momentum carried by the ejected liquid are computed.

Key words: capillary flows, interfacial flows (free surface), thin films

1. Introduction

Among the configurations proposed by Felix Savart to study the nature of microscopic liquid cohesion and its consequences on the macroscopic world is that of a jet impacting normally onto a small solid disk (Savart 1833). At impact, the jet deviates in an axisymmetric fashion and feeds a radially expanding sheet which is bordered, at some distance from the impact location, by a rim collecting the liquid. This distance is referred to as the stable radius of the sheet. In the absence of interaction with the surrounding ambient medium (Huang 1970; Villermaux & Clanet 2002; Lhuissier & Villermaux 2009) or heterogeneous hole nucleation processes (Lhuissier & Villermaux 2013) altering the ballistic motion of the liquid in the sheet, this radius has been, following Taylor (1959), conveniently represented as an equilibrium between the inertia of the flow and capillarity retraction (Clanet & Villermaux 2002; Villermaux, Pistre & Lhuissier 2013). The sheet rim is, in this picture, a stagnation point: for a jet with diameter d and velocity u, due to mass

† Institut Universitaire de France, Paris, France. Email address for correspondence: villermaux@irphe.univ-mrs.fr

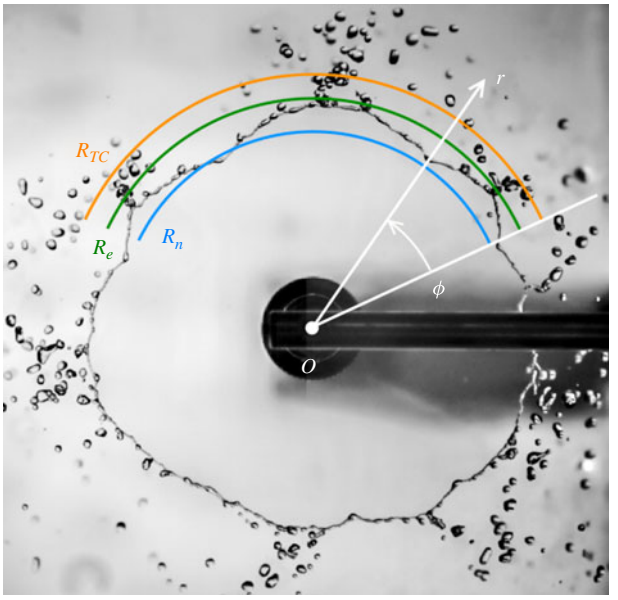

FIGURE 1. Perpendicular view of a water Savart sheet illustrating the regularly spaced cusp-shaped indentations at the edge. The water impacts at O and flows radially until it collects in the liquid rim that borders the sheet. 'Nodes', i.e. bulges in the rim, form at the stagnation points of the flow, at the local minima R_n of the sheet radius, ϕ is the angle between two adjacent nodes. The liquid is ejected from the sheet at the extremities of the cusps, at local maxima R_e smaller than the Culick–Taylor radius R_{TC}. The white dot at O has the same diameter $d = 3$ mm as the jet, and the impact velocity is $u = 2.91$ m s^{-1}. This corresponds to a Weber number $We = \rho u^2 d/\sigma = 353$, where $\rho = 998$ kg m^{-3} and $\sigma = 72$ mN m^{-1} respectively stand for the density and the surface tension of the liquid.

conservation and to the fact that the liquid velocity is preserved along the radial direction r, the sheet thickness h is

$$h = \frac{d^2}{8r}. \tag{1.1}$$

By balancing the capillary retraction force 2σ with the incident momentum flux $\rho h u^2$ (Taylor 1959; Culick 1960), one obtains the radius R_{TC} where all the liquid inertia would be arrested as

$$R_{TC} = \frac{\rho u^2 d^2}{16\sigma} = \frac{We}{16}\, d, \tag{1.2}$$

where we have introduced the Weber number $We = \rho u^2 d/\sigma$, where ρ and σ respectively stand for the density and the surface tension of the liquid.

If this simple picture offers a good representation of the typical size of the sheet and of its dependence on We, it is also known to be inaccurate (Clanet & Villermaux 2002), the mean sheet radius being observed to be somewhat smaller than anticipated in (1.2), and to be at odds with several crucial phenomena. It, first, disregards the actual shape of water sheets, which are obviously not circular, as successively observed by Savart (1833), Taylor (1959), Huang (1970) and Clanet & Villermaux (2002), and as illustrated in figure 1. Second, and more fundamentally, this picture ignores the crucial question of the mass balance at the rim, that is the mechanism

by which the liquid is ejected from the sheet, at its edge. This mechanism must be intrinsically coupled to the details of the sheet shape, and it is clear that a pure stagnation point representation, if it satisfies momentum balance, avoids the question of mass conservation. Moreover, in the case of negligible viscosity that we are considering here (see Villermaux *et al.* (2013) for the corresponding corrections), the mechanism by which the liquid is ejected not only influences the circularity, but also determines the residual radial velocity of the liquid being ejected at the sheet edge, which has been shown to be a small but non-vanishing fraction of the initial velocity in the sheet (Clanet & Villermaux 2002), suggesting that a naive stagnation point picture is ill founded.

These fundamental questions are precisely the motivation for the present study. We first describe in § 2 the shape and the dynamics of the liquid structures bordering the sheet rim. We then rationalize their (stationary) shape and total number around the sheet in § 3. The corresponding model predicts the number of sites of ejection of the liquid, together with its residual velocity as a function of the Weber number, and explains why the radius at which ejection occurs is smaller than R_{TC}. Perspectives are outlined in the conclusion in § 4, as well as the influence of liquid viscosity and of gravity.

2. Phenomenology

The liquid sheet is formed by letting a vertical water jet, with a diameter $d = 3$ mm, impact perpendicularly onto a solid target. The target is a flat disk, with a diameter of 6 mm, surrounded by a thin corona whose vertical offset with respect to the disk surface is tuned so as to ensure a right-angle deflection of the jet at impact (see Clanet & Villermaux 2002). This forms a flat horizontal liquid sheet with radial flow provided $We \gg 1$, as shown in figure 1, where the sheet is seen from the top. The phenomena we describe here are insensitive to ambient air as long as $We < 1000$.

The sheet is certainly not exactly circular. Its edge develops regularly spaced cusp-shaped indentations which result from the self-adaptation of the rim to the liquid flow which transits through it.

The liquid is mainly ejected at localized 'ejection sites', which are approximately evenly distributed along the sheet edge. These sites are located at the tips of the indentations, at the local maxima of the sheet radius. On average, they lie on a circle with radius R_e, which is always smaller than the Taylor–Culick radius R_{TC}. At these sites, the liquid is drained out of the rim by outward jets visible in figure 2, which readily fragment into drops, as seen in figure 1. The existence of this radial motion demonstrates that not all of the momentum of the liquid is dissipated at the edge of the sheet, as already reported by Clanet & Villermaux (2002): the liquid is ejected with a small, but finite, residual velocity.

At the base of the indentations, that is at the minimum radius between two adjacent ejection sites, the rim develops quasi-stationary bulges, which we call 'nodes' because of their shape, as shown in the magnified views of figure 2. These nodes are on average located at a radius R_n such that (figure 1)

$$R_n < R_e < R_{TC}. \tag{2.1}$$

The nodes connect the two inclined portions of the rim in which the liquid flows towards the neighbouring ejection sites. They are actually the nub of the problem we are considering, since their number sets the number of ejection sites and their positions influence the size of the sheet. Their particular importance arises from the

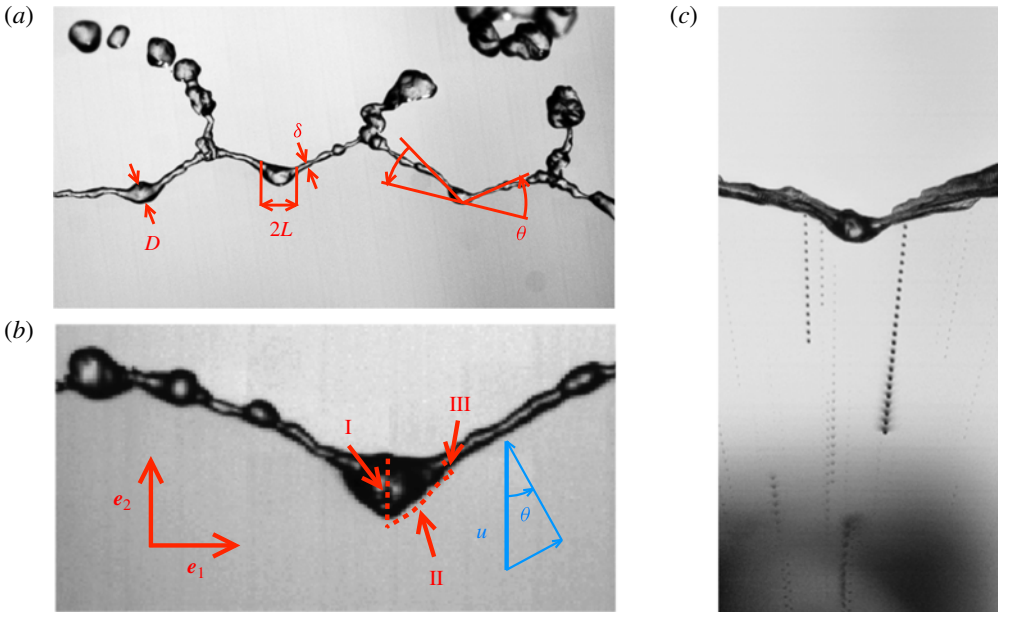

FIGURE 2. (*a*) Details of the sheet edge and definition of the length scales. The liquid rim attached to the edge develops a quasi-steady shape with regularly spaced nodes and ejection sites ($We = 592$ and the image height is 38.6 mm). (*b*) Magnified view of a node showing the control sections I, II and III of the momentum balance at the node. The velocity components parallel and perpendicular to the rim are $u \sin\theta$ and $u \cos\theta$ respectively ($We = 579$ and the image height is 13.5 mm). (*c*) Superposition of 25 images equally spaced in time by 200 μs. The trajectory of the dark small particles in the sheet illustrates the constancy of the liquid velocity, in norm and direction, up to the rim ($We = 303$ and the image height is 36.7 mm).

fact that they are the only portions of the rim that are perpendicular to the radial flow of the sheet, the other portions being either inclined or the bases of jets ejecting drops. The nodes are therefore the only stagnation points of the flow at the edge.

The indentations are not stationary. They are dynamic structures which evolve in time, are born, move and die randomly along the sheet edge. However, their lifetime is much longer than the transit time of the liquid particles flowing through them (see figure 2*c*), and for these particles, they thus appear as frozen stationary structures, an observation we will use in § 3. The number of these indentations is not fixed. It fluctuates slightly, as a consequence of the permanent annihilation and inception of new nodes, around a mean value N, a function of the Weber number. Figure 3 illustrates this dynamics. When two adjacent nodes closely approach each other, they merge, and N decreases by a unit (figure 3*a*). When two adjacent nodes get too distant from each other, a new node forms on one of the large corrugations which develop on the long rim portions that separate the nodes from the next ejection sites, and N increases by a unit (figure 3*b*). The newly nucleated node subsequently grows and recedes toward the sheet centre until it reaches the same radius R_n as the other nodes. The number N is determined by the density of nodes for which the annihilation rate equilibrates the inception rate. The equilibrium is stable, and the global annihilation/inception dynamics maintains a self-sustained population of nodes at the edge of the sheet.

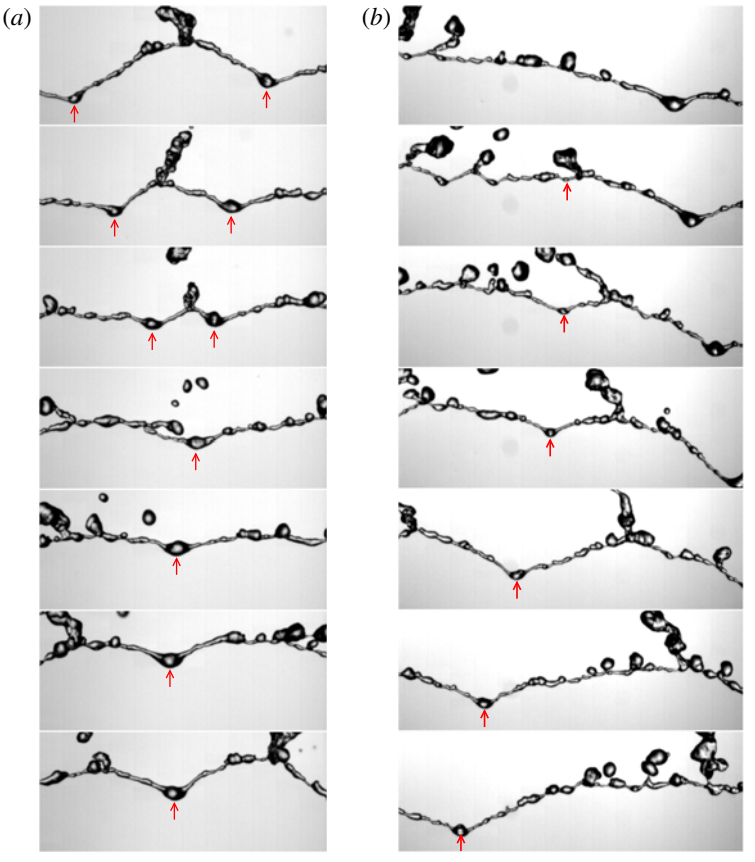

FIGURE 3. Annihilation and inception of the nodes. The time lapse between successive images is 18.5 ms and the height of each image is 12.7 mm. (*a*) When two nodes approach each other closely, they either merge or one of them disappears due to the close interaction with the other node ($We = 463$). (*b*) When neighbouring nodes become too distant from each other, a new node appears due to the corrugations which develop over the long rim portions ($We = 569$).

We emphasize that these indentations are intrinsic to the dynamics of the sheet edge and are not the result of any extrinsic forcing. The fact that they have random and moving locations on the edge means that they do not result from some asymmetries in the jet or in the impact disk, unlike in the study of Taylor (1959), where the location and number of the cusps was forced by imposing large-amplitude azimuthal modulations of the sheet thickness (see also Dressaire *et al.* 2013). This was checked by rotating either the jet, the impact disk, or both, and noticing that the indentations behave independently. They are also not artificial indentations such as those generated by Clanet & Villermaux (2002), using a trick pioneered by Savart himself, consisting in placing a thin wire across the sheet, slicing it at a predetermined radial location.

3. The structure of the cusps

The indentations of the sheet edge described in figure 2 are quasi-steady structures composed of a node located at $r = R_n$ plus the associated two oblique rim portions departing from it. These rim portions, oriented at an angle $\pi/2 - \theta$ with respect to

the direction of the incident flow (direction $\boldsymbol{e_2}$), collide at a radial position $r = R_e$. The merging of each pair of rim portions coming from adjacent nodes creates $N = 2\pi/\phi$ ejection sites from which the liquid is expelled radially outwards, where ϕ denotes the angle between two consecutive nodes (see figure 1).

To understand the structure of a cusp, it is first essential to note from figure 2(*c*) that, upstream of the nodes, fluid particles follow a purely radial ballistic trajectory. There is no feedback coupling of the sheet edge shape, orientation or position on the flow in the sheet. The rim portions are oblique shock waves, and the local equilibrium describing the overall structure of a cusp, namely R_n and ϕ, solely relies on the unperturbed velocity u and sheet thickness $h(r)$ in its vicinity, as given in (1.1). In order to determine this structure, we now consider a control volume containing a node and delimited by the sections I, II and III sketched in figure 2(*b*). The net force exerted at surfaces I–III orients the liquid momentum flux entering this volume, through II, towards the direction of the rim, emanating from III. Defining $h_n = h(R_n)$, $2L$ and D as the sheet thickness at the radial position of the node, the node width and its diameter in the plane of symmetry (see figure 2*c*), respectively, the forces involved in this balance are as follows.

(*a*) The net force at I, that is, across the plane of symmetry of the node, is the sum of the capillary force along the node perimeter $-\pi D\sigma\, \boldsymbol{e_1}$ and of the pressure force $(\pi D^2/4)p_{\rm II}\, \boldsymbol{e_1}$, where $p_{\rm II} \simeq 2\sigma/D$ denotes the liquid pressure in the node.

(*b*) The momentum flux and the capillary force at II are respectively given by $\rho u^2 L h_n\, \boldsymbol{e_2}$ and $2\sigma L\, (\boldsymbol{e_1} + \boldsymbol{e_2})$, where it has been taken into account that the projected lengths of surface II on the directions $\boldsymbol{e_1}$ and $\boldsymbol{e_2}$ are both approximately of order L.

(*c*) Lastly, the capillary force and the pressure force in the rim, at III, are $\pi\delta\sigma\ (\sin\theta\, \boldsymbol{e_2} + \cos\theta\, \boldsymbol{e_1})$ and $-(\pi\delta^2/4)p_{\rm III}\ (\sin\theta\, \boldsymbol{e_2} + \cos\theta\, \boldsymbol{e_1})$ respectively, where δ is the diameter of the rim and $p_{\rm III} \simeq 2\sigma/\delta$ is the capillary pressure in it. The momentum flux through III is still an unknown $\boldsymbol{m}$ to be determined as a result of the momentum balance at the node.

Figure 3 shows that the bulge at the node is a long-lived structure slowly growing from the capillary destabilization of the rim. The relative dimensions of the bulge L and D must thus be such that it is a marginally stable object with respect to capillary destabilization in the sense of Plateau (Plateau 1873). Representing the node as a cylinder of length $2L$ and radius $D/2$, and expressing the Plateau condition for marginal stability $(2\pi/2L)\,(D/2) = 1$, we have

$$L \simeq \pi D/2. \tag{3.1}$$

Shorter bulges expand by capillary pressure, and longer bulges break through the capillary instability. This is in fair agreement with the measurements of figure 4(*a*) showing that L and D are of the same order of magnitude, and are both much larger (typically 100 times larger) than the sheet thickness h_n to which the bulge is attached.

The fluid particles entering the bulge are reoriented in the direction of the oblique rim portions. Mass conservation thus provides the value of the rim diameter δ as

$$u h_n L \simeq (\pi\delta^2/4) u \sin\theta, \tag{3.2}$$

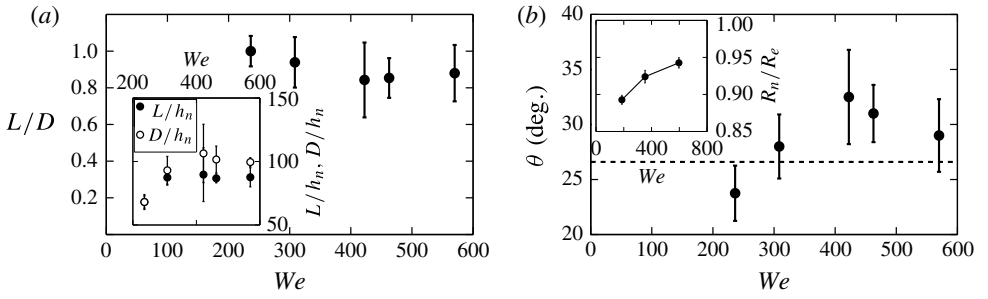

FIGURE 4. (*a*) Ratio of the half-width L to the diameter D of the node (see figure 2) versus We. The inset shows L and D scaled by the sheet thickness at the node h_n. (*b*) Angle θ of the rim at the nodes (as defined in figure 2) versus We. The dashed line represents $\theta = 26.6^\circ$ derived in (3.6). The inset shows that R_n tends to R_e as We increases.

since the velocity in the rim at the bulge exit is approximately given by $u \sin\theta$. Due to the fact that the contributions of both the capillary and the pressure forces in region III can be neglected with respect to those in region I, an approximation that will be justified *a posteriori*, the momentum exiting the node through III is then, at leading order,

$$\begin{aligned} \boldsymbol{m} &\simeq \rho u^2 h_n L \boldsymbol{e_2} - 2\sigma L \boldsymbol{e_2} + 2\sigma L \boldsymbol{e_1} - \pi D \sigma \boldsymbol{e_1} + \frac{\pi D}{2}\sigma \boldsymbol{e_1} \\ &= \rho u^2 h_n L \boldsymbol{e_2} - 2\sigma L \boldsymbol{e_2} + \sigma L \boldsymbol{e_1}. \end{aligned} \tag{3.3}$$

Now, θ and h_n are also linked by the condition that the momentum flux $\rho u^2 h_n \cos^2\theta$ absorbed per unit length of the rim is approximately balanced by the capillary forces 2σ acting perpendicular to the rim; in other words, the rim orientation satisfies the condition for a stationary inclined shock. This is the Taylor (1959) 'stagnation point' representation, omitting the contribution of the centrifugal forces and rim bending due to the accumulation of momentum from the incoming sheet flow, the neglect of which is justified below. Thus, within relative errors to be determined, the momentum balance in the direction perpendicular to the shock yields

$$\cos^2\theta = \frac{2\sigma}{\rho u^2 h_n} \quad \text{or} \quad \tan\theta = \sqrt{\frac{\rho u^2 h_n}{2\sigma} - 1}. \tag{3.4a,b}$$

Consequently, since the momentum flux exiting the node has the same direction as that of the rim, it follows from (3.3) and (3.4) that

$$\begin{aligned} \tan\theta &= \frac{\boldsymbol{m}\cdot\boldsymbol{e_2}}{\boldsymbol{m}\cdot\boldsymbol{e_1}} \\ &= \frac{\rho u^2 h_n/2\sigma - 1}{1/2} = \frac{\tan^2\theta}{1/2}. \end{aligned} \tag{3.5}$$

This gives

$$\tan\theta = 1/2, \quad \text{that is } \theta \simeq 26.6^\circ, \tag{3.6}$$

a value for the cusp angle at the node θ that matches the measurements reported in figure 4(*b*). Finally, making use of relations (1.1), (1.2), (3.4) and (3.6), the radial position of the node is expressed as a function of the Taylor–Culick radius as

$$\frac{1}{\cos^2\theta} = \frac{\rho u^2 d^2}{16\sigma R_n} = \frac{5}{4}, \tag{3.7}$$

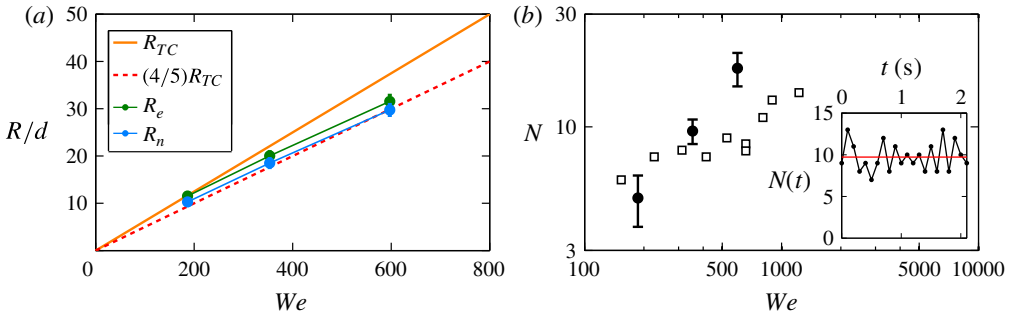

FIGURE 5. (*a*) Average radius of the nodes and of the cusp extremities versus *We*. The orange solid line shows the Taylor–Culick radius. The red dashed line is $(4/5)R_{TC}$ from (3.8). (*b*) Mean number of ejection sites N at the edge of the sheet versus *We*. (•) present study, (□) data from figure 12 in Clanet & Villermaux (2002). The error bars stand for the standard deviation of N, the temporal fluctuation of which is shown in the inset for $We = 353$.

which yields the radius of the nodes

$$R_n = \frac{4}{5} R_{TC}, \tag{3.8}$$

representing well the measurements in figure 5(*a*). The relative errors made in this representation are weak. Since $\sin\theta \simeq 1/2$, it follows from (3.2) that $\delta/L \simeq \sqrt{(8/\pi)h_n/L} \simeq 0.16$ (see figures 2 and 4). Therefore, the ratios in each direction $\boldsymbol{e_1}$ and $\boldsymbol{e_2}$ of the resulting capillary forces acting at the node surface III $\pi\delta\sigma/2\,(\sin\theta\,\boldsymbol{e_2} + \cos\theta\,\boldsymbol{e_1})$, with respect to the net capillary force acting at surfaces I and II, namely, $-2\sigma L\boldsymbol{e_2} + \sigma L\boldsymbol{e_1}$, are given respectively by $\delta/L\,(\pi/2)\cos\theta \simeq 0.2$ and $\delta/L\,(\pi/4)\sin\theta \simeq 0.06$, justifying why they were neglected in (3.3). The centrifugal force in the balance of momentum perpendicular to the rim at the bulge exit is $\rho u^2 \sin^2\theta\,\delta^2/R_n \sim |\boldsymbol{m}|/R_n \sim \sigma L/R_n$. Thus, since the capillary force acting normal to the rim is 2σ, the relative error made in the balance (3.4) is of order $L/(2R_n) \ll 1$ (see figure 1), further supporting the approximation made.

We now turn to the ejection radius R_e. Assimilating the rim departing from a node to a straight line (the actual shape is bent slightly inward, see figure 1 and Clanet & Villermaux (2002)) ending at a radius R_e, the angle ϕ in figure 1 is simply expressed as a function of the ratio R_n/R_e according to

$$\frac{R_e}{R_n} = \frac{\cos\theta}{\cos(\theta + \phi/2)}. \tag{3.9}$$

If nothing destabilizes it before that point, the rim will extend down to the unsurpassable Taylor–Culick radius. Imposing, with no justification at this stage, $R_e = R_{TC}$, and making use of $R_n/R_{TC} = \cos^2\theta$ from (3.8), (3.9) reduces to

$$\cos(\theta + \phi/2) = \cos^3\theta. \tag{3.10}$$

With $\theta \simeq 26.6°$, this yields $\phi \simeq 35°$ and $N = 2\pi/\phi \simeq 10$. The measurements of the number of cusps N shown in figure 5(*b*) are somewhat consistent with this value, at least in order of magnitude: there are indeed of the order of 10 cusps around the sheet, but what figure 5(*b*) also shows is a distinctive increase of N with *We*.

The reason for this discrepancy is that the ejection radius R_e is not R_{TC}, as seen in figures 1 and 5(*a*). The liquid is ejected upstream of R_{TC} because, as can be

appreciated from figures 2(*b*) and 3, the growth of capillary perturbations along the rim breaks the latter before it has the chance to reach the Taylor–Culick radius. The rim capillary perturbations grow with a characteristic time $\tau \sim \sqrt{\rho\delta^3/\sigma}$, that is, considering the proportionality of δ to h_n suggested by figure 4(*a*) and (3.2),

$$\tau \sim \sqrt{\frac{\rho h_n^3}{\sigma}}. \tag{3.11}$$

Right after exiting the node, the perturbations are convected along the rim with a velocity $u\sin\theta$ (this velocity is further altered since the rim keeps accumulating mass and momentum down to the ejection site, see, e.g. Bremond & Villermaux (2006)). The arc length between the node and the position where the rim has lost its integrity by capillary instability (and therefore sheds mass, thus defining R_e) is thus expected to decrease with the Weber number as

$$u\sin\theta\,\tau \sim dWe^{-1}. \tag{3.12}$$

The trend of (3.12) is in qualitative agreement with the observation shown in the inset of figure 4(*b*), indicating that R_e tends towards R_n as *We* increases. Since (3.9) expresses that ϕ decreases for increasing R_n/R_e, this explains why the number of cusps N is a growing function of the Weber number: the capillary instability limits the length of the rim earlier for larger *We*.

This capillary instability is, furthermore, appreciably excited by the strong agitation in the rim itself which results from the dissipation of the mechanical energy it absorbs. The hieratic motion of the bulge at the node is, for instance, obvious in figure 3. The rate of energy dissipation u'^3/D, per unit mass ρLD^2 of the bulge, defines a typical turbulent velocity u' which is, equilibrating the kinetic incident energy from the sheet with that dissipated at the bulge location, such that

$$\frac{1}{2}\rho u^2 h_n L u \sim \rho D^2 L \frac{u'^3}{D}, \tag{3.13}$$

hence

$$u' \sim \left(\frac{\sigma u}{\rho D}\right)^{1/3}. \tag{3.14}$$

We have already noted in (3.1) that the bulge aspect ratio L/D is of order unity, since it is a marginally stable structure with respect to the rim capillary instability. We can now estimate its absolute size, or at least give an upper bound for it: it must be such that its internal velocity fluctuations do not break it. Therefore, the Weber number We_c based on D and u' should be at most of order unity, i.e.

$$We_c = \frac{\rho u'^2 D}{\sigma} = \mathcal{O}(1). \tag{3.15}$$

Consequently, by making use of $h_n = 2\sigma/(\rho u^2) \times R_{TC}/R_n$ from (3.4), one anticipates that

$$\frac{D}{h_n} \sim \frac{R_n}{R_{TC}} We_c^3, \tag{3.16}$$

which is essentially a constant, as seen in figure 4(*a*).

4. Conclusion and extensions

The relation in (3.16) completes the description of the cusps bordering stationary radially expanding liquid sheets, for which we have successively given the radius

of the nodes R_n, the shape of the bulges at the nodes L/D, their absolute size D, the distance between the nodes and the radial extremity of the cusps R_e (where the sheet disrupts into drops), and the number of ejection sites N. This answers the long-standing question of the status of these ubiquitous structures.

These cusps are the structures that accommodate for both mass and momentum conservation at the sheet edge when its radius (R_n or R_e) is steady. They are not present on a rim recently formed by, for example, cutting a sheet along a straight line (Lhuissier & Villermaux 2011) or piercing it with a hole. In this early dynamics, the rim collects the liquid of the sheet as it recedes, before instabilities (capillary, centrifugal) destabilize it. The cusps must thus be understood as the saturated late-stage form of the transient natural instabilities the rim undergoes as soon as it is formed, and for which figure 3 illustrates the dynamics. In this respect, they bear obvious similarities to the cusps formed on premixed flame fronts (Michelson & Sivashinsky 1982; D'Angelo, Joulin & Boury 2000; Aldbrege & Killingsworth 2004) and, in general, to fronts that propagate normal to themselves and suffer a geometric Eikonal type of focusing, an analogy which will probably be worth pursuing.

A last, and important, consequence of the present findings is the direct prediction of the ejection velocity of the liquid when it is expelled from the sheet at R_e. Fluid particles flow with an approximate velocity $u \sin\theta$ at the rim junction with the node that slightly varies down to the ejection site due to the mass and momentum accumulation along the rim. This effect is also partly responsible for the rim portions from opposite sides being inclined with an angle smaller than θ (see figure 1). At the extremity of a symmetric cusp, the liquid is thus expelled with a velocity of the order of but smaller than $u \sin^2\theta$ (the collision of the two rims is inelastic). The average radial velocity u_e at which the jets (readily breaking into drops) are ejected from the sheet is thus, using (3.7) and (3.8),

$$\frac{u_e}{u} \lesssim 1 - \frac{R_n}{R_{TC}} = \frac{1}{5}. \tag{4.1}$$

This is in agreement with the measurements in Clanet & Villermaux (2002), showing that the ratio of velocities in (4.1) indeed approaches $1/5$ by slowly increasing with increasing We, consistently with the fact that R_n approaches R_e as We increases (see also figure 4*b*). That ejection velocity is, however, interestingly, practically zero with higher-viscosity liquids. This fact is consistent with the determining role invoked here that is played by the capillary instability, not only because it limits the rim extension once the cusps are formed, but also because it is the source of the cusp nucleation, as explained above. If this instability is damped by viscosity (see, e.g. Eggers & Villermaux 2008), the rim has no chance to grow thickness modulations, i.e. bulges, which are, as figure 3 suggests, necessary for cusp formation. This is why the sheet reaches its maximal extension (itself a function of the impacting Reynolds number, see Villermaux *et al.* (2013)), expelling the liquid with vanishingly small residual radial momentum when the liquid viscosity prevents capillary destabilization of the rim. Once the cusps are formed, however, viscous corrections have little influence on the momentum balance in (3.3): while the contribution of the shear stresses is exactly zero at surface II (see figure 2) since $\partial u/\partial r = 0$ in $r = R_n$, the relative contribution of the viscous stresses at surface III can be safely neglected with respect to that of the momentum flux with the present water sheet since $u\delta/\nu \gtrsim O(10^3)$.

A similar role to that of viscosity is surprisingly played by gravity: our sheet is formed perpendicular to gravity. If it were bent slightly upwards the number of cusps

would reduce, and conversely if it were bent downwards, which makes the value of N extremely sensitive to the horizontality of the sheet, a fact probably responsible for the discrepancy in absolute value between the two data sets reported in figure 5(*b*). We suspect that gravity damps (conversely increases) the rim capillary instability through a Rayleigh–Taylor kind of mechanism, a specific study left for future research.

Acknowledgements

We acknowledge financial support from Institut Carnot STAR under Project AAP-2013 and from the Spanish MINECO under Project DPI2011-28356-C03-01.

References

ALDBREGE, R. C. & KILLINGSWORTH, N. J. 2004 Experimental evaluation of Markstein-number influence on thermoacoustic instability. *Combust. Flame* **137**, 178–197.

BREMOND, N. & VILLERMAUX, E. 2006 Atomization by jet impact. *J. Fluid Mech.* **549**, 273–306.

CLANET, C. & VILLERMAUX, E. 2002 Life of a smooth liquid sheet. *J. Fluid Mech.* **462**, 307–340.

CULICK, F. E. C. 1960 Comments on a ruptured soap film. *J. Appl. Phys.* **31**, 1128–1129.

D'ANGELO, Y., JOULIN, G. & BOURY, G. 2000 On model evolution equations for the whole surface of three-dimensional expanding wrinkled premixed flames. *Combust. Theor. Model.* **4**, 317–338.

DRESSAIRE, E., COURBIN, L., DELANCY, A., ROPER, M. & STONE, H. A. 2013 Study of polygonal water bells: inertia-dominated thin-film flows over microtextured surfaces. *J. Fluid Mech.* **721**, 46–57.

EGGERS, J. & VILLERMAUX, E. 2008 Physics of liquid jets. *Rep. Prog. Phys.* **71**, 036601.

HUANG, J. C. P. 1970 The break-up of axisymmetric liquid sheets. *J. Fluid Mech.* **43**, 305–319.

LHUISSIER, H. & VILLERMAUX, E. 2009 Soap films burst like flapping flags. *Phys. Rev. Lett.* **103**, 054501–(4).

LHUISSIER, H. & VILLERMAUX, E. 2011 The destabilization of an initially thick liquid sheet edge. *Phys. Fluids* **23** (9), 091705; 091704.

LHUISSIER, H. & VILLERMAUX, E. 2013 'Effervescent' atomization in two dimensions. *J. Fluid Mech.* **714**, 361–392.

MICHELSON, D. M. & SIVASHINSKY, G. I. 1982 Thermal-expansion induced cellular flames. *Combust. Flame* **48**, 211–217.

PLATEAU, J. 1873 *Statique Expérimentale et Théorique des Liquides Soumis aux Seules Forces Moléculaires*. Gauthiers Villars.

SAVART, F. 1833 Mémoire sur la constitution des Veines liquides lancées par des orifices circulaires en mince paroi. *Ann. Chim. France* **53**, 337–386.

TAYLOR, G. I. 1959 The dynamics of thin sheets of fluid. II. Waves on fluid sheets. *Proc. R. Soc.* A **253** (1274), 296–312.

VILLERMAUX, E. & CLANET, C. 2002 Life of a flapping liquid sheet. *J. Fluid Mech.* **462**, 342–363.

VILLERMAUX, E., PISTRE, V. & LHUISSIER, H. 2013 The viscous Savart sheet. *J. Fluid Mech.* **730**, 607–625.